

# Nonaxisymmetric Shapes of Biological Membranes from Locally Induced Curvature

Yannick A. D. Omar,<sup>1,\*</sup> Amaresh Sahu,<sup>1,\*</sup> Roger A. Sauer,<sup>2,\*</sup> and Kranthi K. Mandadapu<sup>1,3,\*</sup>

<sup>1</sup>Department of Chemical and Biomolecular Engineering, University of California, Berkeley, California; <sup>2</sup>Aachen Institute for Advanced Study in Computational Engineering Science, RWTH Aachen University, Aachen, Germany; and <sup>3</sup>Chemical Sciences Division, Lawrence Berkeley National Laboratory, Berkeley, California

**ABSTRACT** In various biological processes such as endocytosis and caveolae formation, the cell membrane is locally deformed into curved morphologies. Previous models to study membrane morphologies resulting from locally induced curvature often only consider the possibility of axisymmetric shapes—an indeed unphysical constraint. Past studies predict that the cell membrane buds at low resting tensions and stalls at a flat pit at high resting tensions. In this work, we lift the restriction to axisymmetry to study all possible membrane morphologies. Only if the resting tension of the membrane is low, we reproduce axisymmetric membrane morphologies. When the resting tension is moderate to high, we show that 1) axisymmetric membrane pits are unstable and 2) nonaxisymmetric ridge-shaped structures are energetically favorable. Furthermore, we find the interplay between intramembrane viscous flow and the rate of induced curvature affects the membrane's ability to transition into nonaxisymmetric ridges and axisymmetric buds. In particular, we show that axisymmetric buds are favored when the induced curvature is rapidly increased, whereas nonaxisymmetric ridges are favored when the curvature is slowly increased. Our results hold relevant implications for biological processes such as endocytosis and physical phenomena like phase separation in lipid bilayers.

**SIGNIFICANCE** Locally induced curvature is essential in a variety of biological processes. For example, in endocytosis, the cell membrane forms small invaginations which then develop into mature buds. In this study, we use recent advances in modeling lipid membranes to investigate the morphologies arising from locally induced curvature under varying membrane tension. We find that low membrane tensions result in axisymmetric, bud-shaped morphologies. However, at high membrane tensions, we find that locally induced curvature leads to the formation of shallow, nonaxisymmetric, cylindrically shaped “ridges,” which are energetically favorable compared with axisymmetric morphologies. Our general nonaxisymmetric studies reveal symmetry-breaking morphological transitions inherent to lipid membranes and hold implications for biological processes as well as physical phenomena including phase separation.

## INTRODUCTION

The cell and its organelles are marked by a variety of strongly curved and dynamic boundaries at which local curvature induction is vital. For instance, the cell membrane forms spherical vesicles as an important means of trafficking (1), the endoplasmic reticulum maintains but also dynamically remodels networks of tubules (2,3), and caveolae form curved pits that can disassemble under increased tension (4). Endocytosis is another prominent biological process in which curvature is locally induced. During endocytosis, proteins bend

the cell membrane through different mechanisms such as scaffolding and protein insertion (5–8). Other processes that can induce spatially varying curvatures are, for instance, charge deposition on one of the lipid monolayers (9), spatial variations of the lipid composition through phase separation (10), and the formation of block liposomes (11). The examples given above show the significance of locally induced curvature in synthetic and biological systems.

Although local curvature induction in lipid membranes is known to play an important role in many biological systems, the physics underlying such phenomena is not well-understood. Theoretical and numerical studies are required to gain deeper insight into such processes; however, the time-scale for phenomena involving local curvature induction is often on the order of seconds (12–14), and the corresponding deformations range over lengths of 100–1000 nm

Submitted September 9, 2019, and accepted for publication July 15, 2020.

\*Correspondence: [yannick.omar@berkeley.edu](mailto:yannick.omar@berkeley.edu) or [amaresh.sahu@berkeley.edu](mailto:amaresh.sahu@berkeley.edu) or [sauer@aices.rwth-aachen.de](mailto:sauer@aices.rwth-aachen.de) or [kranthi@berkeley.edu](mailto:kranthi@berkeley.edu)

Editor: Markus Deserno.

<https://doi.org/10.1016/j.bpj.2020.07.021>

© 2020 Biophysical Society.



(5,12,15). Such length and timescales cannot be resolved using molecular simulation methods, and hence, a continuum approach is often employed to understand membrane-mediated processes involving locally induced curvature.

Using a continuum approach, many studies successfully modeled shape changes in lipid membranes. The continuum model commonly used for lipid bilayers is developed in the seminal contributions by Canham (16), Helfrich (17), and Evans (18) and can be considered an extension of Naghdi's work on shell theory (19). Since these pioneering developments, this model and its extensions reproduced many experimentally observed morphologies of lipid vesicles (20–23), including tubule formation from giant unilamellar vesicles (24,25).

Many works also studied the effects of isotropic, locally induced curvature on lipid membranes. Continuum models were used in a variety of contexts, including in the study of compositional asymmetry during phase separation (26–30) and protein-induced curvature (31–35). Biological processes such as lipid droplet formation (36,37) and endocytosis (32,38–44) were also modeled via locally induced curvature in previous studies. However, because of the mathematical and numerical complexity of modeling lipid membrane dynamics, most of the aforementioned continuum studies do not allow for arbitrary deformations. Instead, they are often restricted to axisymmetric shapes or small deviations from fixed geometries such as planes, cylinders, or spheres. Such studies do not capture arbitrary morphological changes occurring between different geometries. Moreover, many of these studies ignore the interplay between induced curvature and intramembrane viscous flow.

Alternative approaches to the deterministic, continuum approach to simulate locally induced curvature on the spatial and temporal scales considered in this manuscript are provided by a large body of work based on the framework of statistical mechanics. Statistical mechanics models are usually less restricted in the permissible deformations but are not guaranteed to rigorously model the in-plane fluidity of the membrane. Additionally, the surface tension is often treated in terms of the excess area—a perspective different from the one employed in this manuscript. Nonetheless, many biological phenomena have been successfully investigated using statistical mechanics models, including phase separation (45–48) and protein-induced budding (49–53) (see also (54,55) for reviews).

This study is based on recent theoretical advances in the continuum description of lipid membranes (56–59) and corresponding numerical developments employing finite element methods, all within the setting of differential geometry (60–64). These developments capture the coupling between elastic out-of-plane bending and nonequilibrium processes such as intramembrane fluid flow, intramembrane phase transitions, and chemical reactions on arbitrarily curved and deforming lipid bilayers. Many biological phe-

nomena are indeed governed by out-of-equilibrium effects, and these recent advances allow us to explore the underlying physics of a variety of such phenomena. Here, we focus on the intricate coupling between in-plane flow and out-of-plane deformations—a coupling that is known to be important in systems of biological relevance (56,63,65) and yet is often neglected.

In this study, we investigate the membrane morphologies of an initially flat membrane patch with a nonzero spontaneous curvature in the center. We distinguish between axisymmetric morphologies such as circular pits and buds, observed during the early and late stages of endocytosis, respectively, and nonaxisymmetric, ridge-like morphologies that resemble eisosomes in yeast cells. We show that axisymmetric membrane morphologies are only preserved if the resting tension of the membrane is low. When the resting tension is high, we show that 1) axisymmetric invaginations are unstable and 2) nonaxisymmetric ridge-shaped structures are energetically favorable. We study the dynamical effects resulting from the interplay between intramembrane viscous flow and induced curvature and find the rate at which the locally induced curvature increases is a key determinant in the formation of ridges. In particular, we show that axisymmetric buds are favored when the induced curvature is rapidly increased, whereas nonaxisymmetric ridges are favored when the curvature is slowly increased—the rate of change of induced curvature affects the intramembrane viscous flow of lipids, which can impede the membrane's ability to transition into ridges.

Our work contradicts previous studies of membrane deformations due to locally induced curvature (38,40–43) by showing that the assumption of axisymmetry is not generally valid when studying locally induced curvature. It further shows that there exists a physically relevant, nonaxisymmetric mode of deformation that has not been reported before. Our work advances the preliminary findings in (61), in which nonaxisymmetric deformations due to locally induced curvature were first observed. Whereas (61) focused on the development of the numerical method, here we seek to explore the underlying physics and biological implications.

## METHODS

### Theoretical membrane model

In this section, we briefly describe our theoretical model; however, the interested reader is referred to the [Supporting Materials and Methods](#) and (59) for further details. Lipid membranes are unique materials in that they behave like a fluid in-plane yet elastically resist bending out-of-plane. Moreover, lipid bilayers are practically area incompressible (66). We model the lipid membrane as a single two-dimensional manifold about the membrane midplane.

The elastic membrane behavior is governed by the energetic penalty for bending, commonly captured with the Helfrich free energy (17), and the membrane's areal incompressibility. The free energy per unit area is given by

$$w = k_b(H - C)^2 + k_g K + \frac{1}{J}\lambda(J - 1), \quad (1)$$

where  $H$  and  $K$  are the mean and Gaussian curvatures, respectively;  $k_b$  and  $k_g$  are the corresponding mean and Gaussian bending moduli;  $J$  denotes the relative change in surface area with respect to a reference configuration; and  $\lambda$  is the surface tension. The bending rigidities  $k_b$  and  $k_g$  are assumed to be uniform throughout the membrane. In Eq. 1, the first two terms comprise the Helfrich free energy density, and the last term accounts for the incompressibility constraint.

We model the effects of induced curvature with the spontaneous curvature  $C$ , which makes it energetically favorable for the membrane to be curved ( $H \neq 0$ ) whenever  $C \neq 0$ . Additionally, membrane shape changes and spatial variations in the spontaneous curvature drive an in-plane flow of lipids. We model the in-plane flow as that of a two-dimensional Newtonian fluid, which results in additional in-plane viscous stresses (see [Supporting Materials and Methods](#)). Furthermore, we note that in-plane viscous flows are coupled with the out-of-plane membrane motion (56,57,59), leading to an intricate relationship between surface flows, out-of-plane deformations, and surface tension gradients (57,63,65). For the length scales involved in this study, dissipation in the bulk fluid is negligible compared with the in-plane viscous dissipation (56,67,68). Hence, we neglect effects of the bulk fluid surrounding the membrane. Similarly, our model does not account for thermal fluctuations. As is argued in the [Supporting Materials and Methods](#), thermal fluctuations decay quickly compared to the timescales considered here. We also defer studying the effects of intermonolayer slip to future work (56,67).

## Simulation procedure

We employ our recent isogeometric finite element formulation (61) to simulate lipid membranes under the influence of locally induced curvature (see [Supporting Materials and Methods](#) for details). To study the morphologies resulting from locally induced curvature, we consider a model system consisting of a large circular lipid bilayer patch of radius  $L$ , shown in gray in Fig. 1. The outer edge is subjected to a uniform surface tension  $\lambda_0$ , which from now on will be referred to as the “resting tension.” Physically, the resting tension describes the surface tension at equilibrium, which we assume to remain unchanged far away from the region of induced curvature. The surface tension is only prescribed on the boundary and otherwise acts as a Lagrange multiplier to ensure incompressibility of the membrane. This is similar to a reservoir boundary condition in classical fluid mechanics. The outer edge is further pinned in the vertical direction and is constrained to maintain zero slope. We study local curvature induction due to, for instance, binding of proteins from the bulk, aggregation of

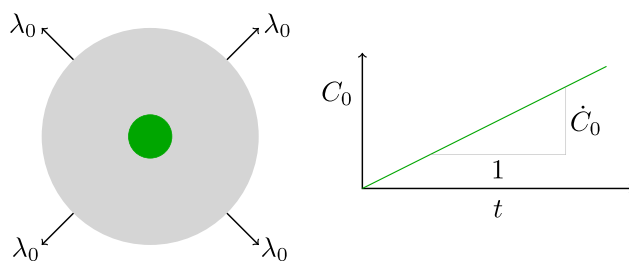


FIGURE 1 The left inset shows the top view of the domain used for our simulations. On the outer boundary, a line tension  $\lambda_0$  is applied to simulate the resting tension far away from the location of curvature induction. A nonzero spontaneous curvature of magnitude  $C_0$  is applied in the center of the circular geometry (shown in green) and is linearly increased over time, as shown in the right inset. To see this figure in color, go online.

proteins, or the change of induced curvature due to remodeling of a protein coat, by imposing a time-dependent, nonzero spontaneous curvature in a circular region in the center of the membrane patch, shown in green in Fig. 1. The central patch, where  $C \neq 0$ , is hereafter referred to as the “coated” region, in reference to a curvature-inducing protein coat as observed, for example, in endocytosis (7). The spontaneous curvature in the coated region, denoted by  $C_0$ , is linearly increased from 0 to  $C_0^{\max}$  over time at a rate  $\dot{C}_0$ , as shown in Fig. 1. The rate  $\dot{C}_0$  captures different rates of protein binding, coat polymerization, or protein aggregation in the coated region and, as we shall show, affects the resulting membrane morphologies.

In our simulations, the coated patch is an ellipse with principal semi-axes of lengths  $a = 1.02R_0$  and  $b = 0.98R_0$ , where  $R_0$  is a length that can be varied. The ellipticity breaks the symmetry of the patch, as is physically the case because of thermal fluctuations and noncircular aggregations of proteins. We ensure our findings are independent of the ellipticity by considering different values of  $a/b$  (see [Supporting Materials and Methods](#)). We assume that the coated region is a material property that is convected with the surface during deformation and neither grows nor diffuses. In doing so, we assume that the coated region neither diffuses as a whole nor grows because of the diffusion of curvature-inducing agents into or out of the coated region. On cell membranes, diffusion may be slow because of a low diffusion coefficient or a favorable chemical potential (59). A detailed motivation for this assumption and criteria when this assumption is valid are provided in the [Supporting Materials and Methods](#).

## RESULTS

### Axisymmetric versus nonaxisymmetric shapes

In what follows, we discuss the possible membrane shapes that can be obtained when the membrane is subjected to local curvature-inducing forces. In biological systems, locally induced curvature often leads to axisymmetric shapes, for example, pits and buds (5,10,14,69). This resulted in a number of studies that exclusively considered axisymmetric shapes (26–29,32,36,38,40–44,70). We will begin by only allowing for axisymmetric shapes as well and will subsequently compare the results to general membrane shapes, not constrained to axisymmetry. We find that when the resting tension is high, the unconstrained membrane shapes are lower in energy and differ significantly from their axisymmetric counterparts. A geometric analysis shows that the unconstrained membrane shapes are shallow cylindrical structures. We end by using energetic arguments to justify why, under certain conditions, the nonaxisymmetric structures are preferred over their axisymmetric counterparts, thus indicating the latter can be unphysical in nature.

In all simulations presented in this section, the spontaneous curvature  $C_0$  is increased from zero to  $C_0^{\max}$  at a constant rate  $\dot{C}_0$  for a given resting tension  $\lambda_0$ . We choose the rate to be  $\dot{C}_0$  (see Table 1), which is small such that the membrane deforms slowly, the in-plane viscosity has a negligible effect on the dynamics, and the membrane generally finds its energy-minimizing configuration. All results shown are instantaneous solutions, i.e., snapshots of an inherently dynamic process. The material and geometric parameters chosen for our simulations are listed in Table 1, which will be used hereafter unless stated otherwise.

**TABLE 1 Model Parameters**

Parameter	Symbol	Value	Reference
Bending rigidity	$k_b$	$30 k_B T$	(84)
Gaussian bending rigidity	$k_g$	$-0.83 k_b$	(85)
Radius of model domain	$L$	1000 nm	
Radius of coated region	$R_0$	100 nm	(86)
In-plane viscosity	$\zeta$	$10^{-8}$ Ns/m	(87)
Low resting tension	$\lambda_0$	$10^{-4}$ pN/nm	(73)
High resting tension	$\lambda_0$	$10^{-1}$ pN/nm	(71)
Maximal spontaneous curvature	$C_0^{\max}$	0.04 1/nm	
Rate of spontaneous curvature	$C_0^0$	$0.001\bar{3}$ 1/(nm s)	(88)

Baseline parameters used for the results of this study unless stated otherwise. The parameters are chosen to be in biologically relevant regimes. Here,  $k_B T = 4.12$  pN nm, where  $k_B$  is the Boltzmann constant and  $T$  is the temperature.

### Axisymmetric solutions

We restrict our general continuum theory (59) to axisymmetry and present a corresponding numerical method following (41) in the [Supporting Materials and Methods](#). In the axisymmetric case, the membrane's radial, axial, and azimuthal velocities are all required to be independent of the azimuthal angle. As opposed to most axisymmetric studies of locally induced membrane curvature (26,27,29,38,40–43,70), we include the viscous forces arising from surface flows during membrane deformation.

Figure 2 shows our axisymmetric results at low and high resting tensions. At the low resting tension  $\lambda_0 = 10^{-4}$  pN/nm, as the spontaneous curvature in the coated region is slowly increased, the membrane first forms an invagination that deepens and eventually deforms into a bud with a con-

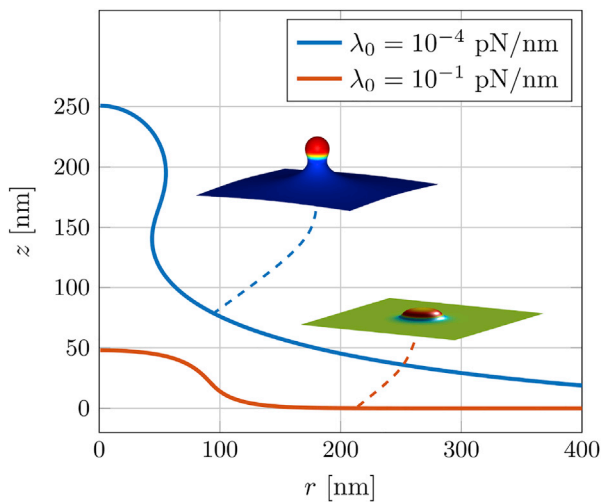


FIGURE 2 Axisymmetric shapes at different resting tensions. At a low resting tension of  $\lambda_0 = 10^{-4}$  pN/nm, the membrane forms a bud ( $C_0 = 0.018$  nm $^{-1}$ , cf. Fig. 3). When the resting tension is high,  $\lambda_0 = 10^{-1}$  pN/nm, the membrane invagination stalls, which results in a shallow, flat pit even at the high spontaneous curvature shown here ( $C_0 = 0.040$  nm $^{-1}$ ). The color of the three-dimensional membrane configurations indicates the mean curvature  $H$ . To see this figure in color, go online.

stricted neck, shown in Fig. 2. On the other hand, at the high resting tension of  $\lambda_0 = 10^{-1}$  pN/nm, the membrane forms a shallow invagination and deforms into a flat, circular pit as the spontaneous curvature is further increased. This can be qualitatively explained by comparing the stored energy in the system based on Eq. 1 and the work required to pull in lipids against the resting tension. When the tension is high, the work required to pull in lipids dominates the energy even when  $H \ll C_0$  in the coated region. Our axisymmetric results reproduce those of earlier studies (41,43) and validate our numerical results.

### Nonaxisymmetric solutions

We next relax the constraint of axisymmetry, thus allowing general membrane deformations, using the finite element formulation developed in (61) (see [Supporting Materials and Methods](#)). We emphasize that our general framework can yield both axisymmetric and nonaxisymmetric solutions. At the low resting tension of  $\lambda_0 = 10^{-4}$  pN/nm, the membrane forms a shallow invagination that deepens into a bud as the spontaneous curvature is increased (Fig. 3 a), similar to the axisymmetric case described above and shown in Fig. 2. In contrast, in the high resting tension case of  $\lambda_0 = 10^{-1}$  pN/nm, the nonaxisymmetric simulations differ strongly from their axisymmetric counterparts. After forming an initially shallow, axisymmetric invagination at low values of  $C_0$ , the membrane deforms into a shallow horizontal ridge (Fig. 3 b). The ridge is aligned along the longer principal axis of the initially elliptic patch. In what follows, we characterize the ridge structure geometrically and then provide energetic arguments why ridges are favored over the stalled, shallow pits observed in axisymmetric simulations.

### Ridge characterization

A more detailed view of the ridge geometry is shown in Fig. 4. The elongated ridge structure has a dumbbell shape and displays reflection symmetry about the principal axes of the coated region. It has a long cylindrical body and terminates in spherical caps, as shown in the zoomed-in view in Fig. 4. To further investigate the ridge geometry and compare it with the spherical buds observed at low resting tension, we plot the two principal curvatures  $\kappa_1$  and  $\kappa_2$  for both ridges and buds (Fig. 5). At low resting tension,  $\kappa_1$  and  $\kappa_2$  take similar values in the budded region, indicating that the bud is nearly spherical.

At high resting tension, on the other hand, the two principal curvatures are of the same order only at early times, when deformations are small (Fig. 5 b, left panels). As soon as the ridge develops, the first principal curvature  $\kappa_1$  decays to a value that is one order of magnitude lower than the second principal curvature  $\kappa_2$ . Such a combination of principal curvatures demonstrates that the ridges are sections of cylindrical structures.

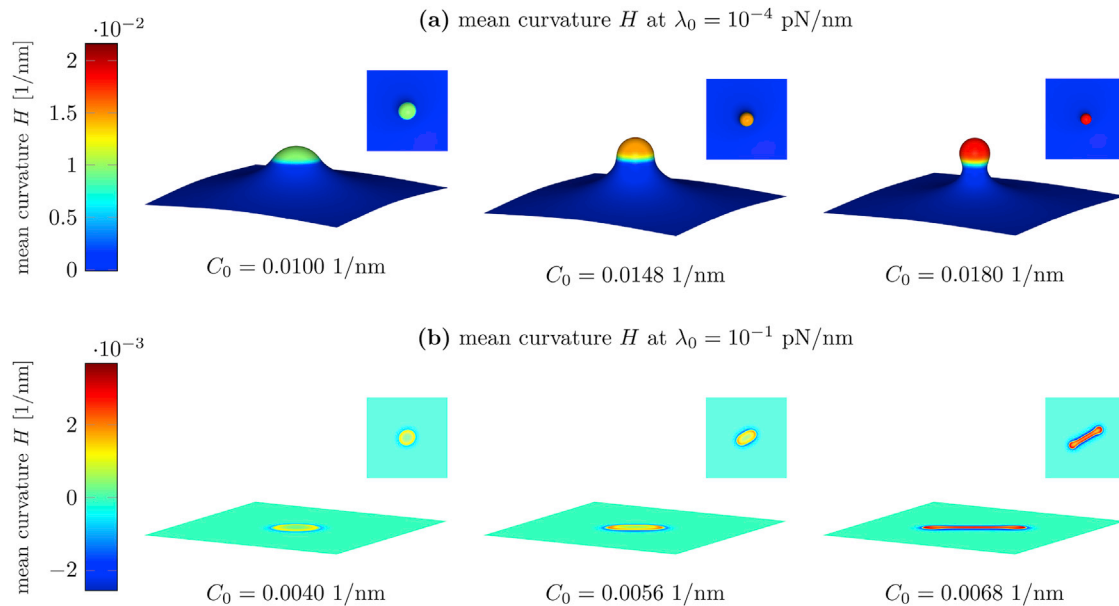


FIGURE 3 Snapshots of membrane shapes at different resting tensions  $\lambda_0$  and different spontaneous curvatures  $C_0$  resulting from nonaxisymmetric simulations. In the low resting tension case of  $\lambda_0 = 10^{-4}$  pN/nm, the nonaxisymmetric solutions resemble the corresponding axisymmetric solutions. In the high resting tension case of  $\lambda_0 = 10^{-1}$  pN/nm, the solution branches out into a nonaxisymmetric, elongated structure, unlike its axisymmetric counterpart. To see this figure in color, go online.

#### Energetic arguments: buds versus ridges

To understand the difference between the axisymmetric and nonaxisymmetric simulations, we consider the total elastic membrane energy

$$\Pi := \int_P w \, da, \quad (2)$$

where  $w$  is the energy density given in Eq. 1 and the area integral is over the membrane patch  $P$ . We can simplify Eq. 2 by recognizing 1) according to the Gauss-Bonnet theorem,

the integral of the term  $k_g K$  over the membrane area is a constant if the boundary remains flat and therefore can be ignored in our case; and 2) the membrane is area incompressible such that the area stretch  $J = 1$  everywhere. Hence, we can redefine the total elastic energy to be

$$\Pi := \int_P k_b (H - C)^2 \, da, \quad (3)$$

such that we only need to take into account the difference between the mean and spontaneous curvature.

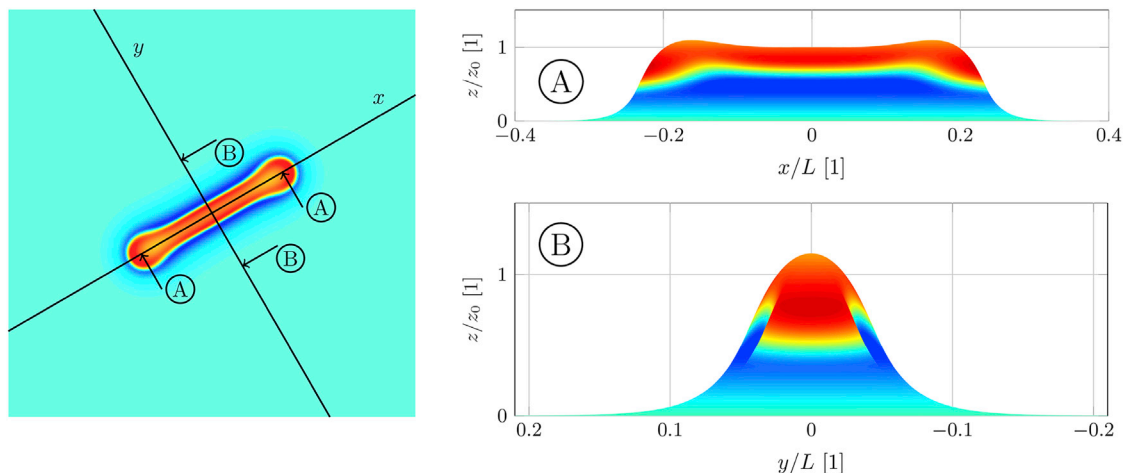


FIGURE 4 Top (left) and cross-sectional (right) views of the ridges forming at high resting tensions. The vertical axis is scaled differently from the horizontal axis, on which  $z_0 := z(x=0, y=0) = 2.6$  nm and  $L = 1000$  nm. Although the geometry is not significantly curved along the longer principal axis (A), it is curved along the shorter principal axis (B), thus resembling a cylinder. Furthermore, the ends of the ridge are spherically shaped. To see this figure in color, go online.

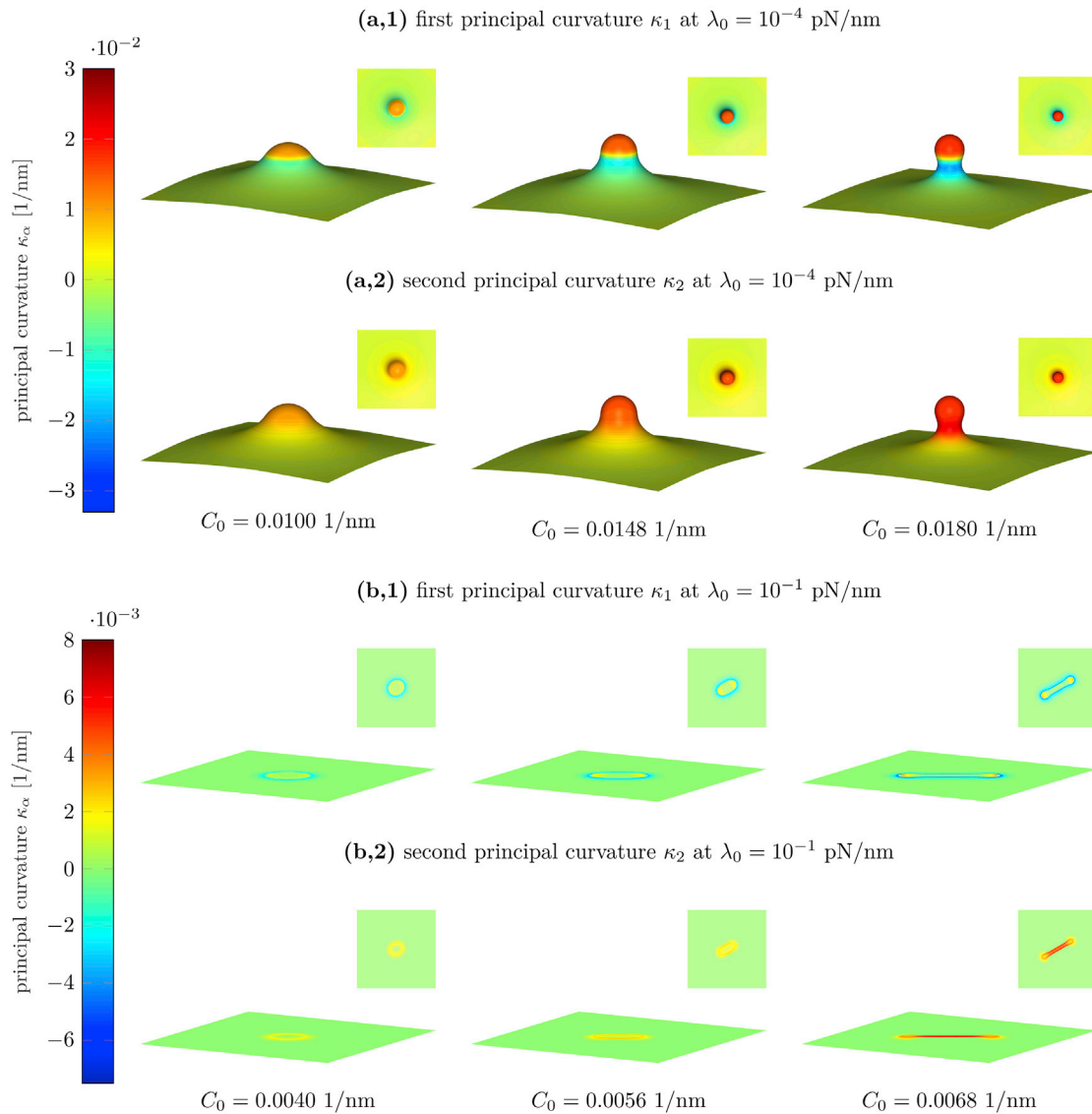


FIGURE 5 Plots of the principal curvatures  $\kappa_1$  and  $\kappa_2$  at different resting tensions  $\lambda_0$  resulting from the nonaxisymmetric problem setup. In the low resting tension case of  $\lambda_0 = 10^{-4}$  pN/nm, the two principal curvatures match in the region of the bud, indicating a spherical shape. In the high resting tension case of  $\lambda_0 = 10^{-1}$  pN/nm, the first principal curvature is one order of magnitude lower than the second principal curvature, indicating a cylindrical shape. To see this figure in color, go online.

Figure 6 shows the elastic energy defined in Eq. 3 for the axisymmetric and nonaxisymmetric membrane shapes. In the low resting tension case, the axisymmetric and nonaxisymmetric energies are almost identical (Fig. 6), and in both cases, a bud forms. However, in the high resting tension case, the axisymmetric and nonaxisymmetric energies only agree at low values of  $C_0$ . At higher spontaneous curvatures, a ridge develops, which is lower in energy than the axisymmetric stalled pit (Fig. 6).

At this point, we provide arguments as to why ridges are possible structures in addition to buds. We begin by splitting the total membrane energy (3) into its contributions from the coated and noncoated regions, where

$$\Pi_{\text{coat}} := \int_{P_{\text{coat}}} k_b (H - C)^2 da \quad (4)$$

and  $P_{\text{coat}}$  is the coated region of the membrane patch. In the coated region, we observe that  $H \approx C_0$  around the resting tension and spontaneous curvature at which the membrane transitions from shallow pits to either buds or ridges. We recognize that the coat energy is minimized when  $H = (1/2)(\kappa_1 + \kappa_2) \approx C_0$ . This is possible in two different ways:

$$\kappa_1 \approx \kappa_2 \approx C_0 \text{ (spherical buds)} \quad (5)$$

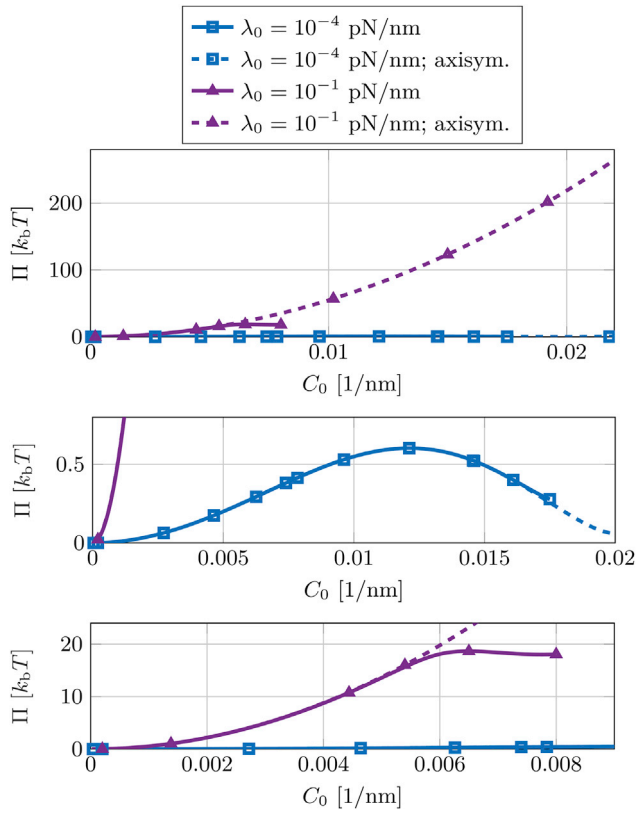


FIGURE 6 Comparison of the elastic energy  $\Pi$  defined in Eq. 3 for the axisymmetric and nonaxisymmetric cases. The two bottom figures show close-ups of sections of the top figure. At a low resting tension of  $\lambda_0 = 10^{-4}$  pN/nm, the stored energies in the two cases match closely. At a high surface tension of  $\lambda_0 = 10^{-1}$  pN/nm, the nonaxisymmetric branch deviates from the axisymmetric case and follows a path with a significantly lower energy than the axisymmetric solution. Data are plotted only until  $C_0 = 0.008 \text{ nm}^{-1}$ , for which the membrane forms a long ridge as shown in Figs. 2 and 5 b. At larger values of  $C_0$ , our simulations are no longer converged under mesh refinement and are thus omitted here (see Supporting Materials and Methods). The line markers merely indicate that the plots are generated from discrete data points, where, for clarity, the number of line markers is much less than the number of data points. To see this figure in color, go online.

or

$$\kappa_1 \approx 0, \kappa_2 \approx 2C_0 \text{ (cylindrical ridges)}. \quad (6)$$

Both choices are available to nonaxisymmetric simulations, whereas only Eq. 5 is compatible with the requirement of axisymmetry. Equation 5 leads to spherical buds and is preferred at low tensions in both the axisymmetric and general cases. On the other hand, Eq. 6 leads to cylindrical ridges and is preferred at high tensions, as seen in Fig. 5. To understand why axisymmetric buds or nonaxisymmetric ridges are preferred, we need to consider both the stored elastic energy and the work done to draw in lipids against the resting tension at the boundary. To this end, we define the latter as

$$W_{\lambda_0} := - \int_{\partial P} \mathbf{u} \cdot \lambda_0 \boldsymbol{\nu} ds, \quad (7)$$

where  $\mathbf{u}$  is the displacement of a point on the boundary;  $\boldsymbol{\nu}$  is the in-plane, outward-pointing normal; and the integral is over the boundary of the membrane patch. Minimization of  $(\Pi + W_{\lambda_0})$  provides the criterion for the formation of nonaxisymmetric ridges or axisymmetric buds. When the resting tension is low, lipids are drawn in radially to form a bud, as is shown in Fig. 7. When the resting tension is high, however, the work required to radially draw in lipids is increased, and therefore, bud formation is hindered and  $\Pi$  increases. Figure 6 shows that ridge formation then lowers the stored energy  $\Pi$ . The formation of ridges is facilitated by a flow pattern that resembles purely extensional flow, as is shown in Fig. 7.

The above argument is heuristic, and the transition from invaginations into spherical buds or cylindrical ridges is marked by an instability (see Supporting Materials and Methods). Although the existence of this instability is deduced entirely from numerical experiments, we aim to present a detailed theoretical stability analysis in a future contribution. In particular, we seek to understand under which conditions spherical buds or cylindrical ridges form, as both can minimize the elastic energy in the coated region (see Eqs. 5 and 6).

Nevertheless, at high resting tensions, we observe ridges instead of axisymmetric buds, indicating that ridges minimize  $(\Pi + W_{\lambda_0})$  at high resting tensions. Accordingly, we can conclude that the axisymmetric results previously found at high resting tensions (41,43) are unstable and unphysical.

## Morphological “phase” diagrams

All of the results presented thus far were generated for a single coat radius  $R_0$ , with the spontaneous curvature ramped up at a single rate  $\dot{C}_0^0$ . In this section, we explore the different morphologies accessible to lipid membranes for a range of parameters in both axisymmetric and nonaxisymmetric settings. In particular, we study morphological “phase” diagrams, for which we consider systems 1) with different coat radii  $R_0$ , 2) over a range of resting tensions  $\lambda_0$ , and 3) with different rates of change of spontaneous curvature  $\dot{C}_0$ . We find that increasing the spontaneous curvature quickly can lead to an interplay between in-plane viscous forces and out-of-plane deformations, which prevent the membrane from reaching its lowest-energy configurations, thus affecting the transition into ridges described above. A classification of the morphologies observed in simulations is provided in Fig. 8.

### Geometry effects: $R_0$ vs. $C_0$

We first examine how different coat radii can affect membrane morphology. As shown in Fig. 9, the coat radius

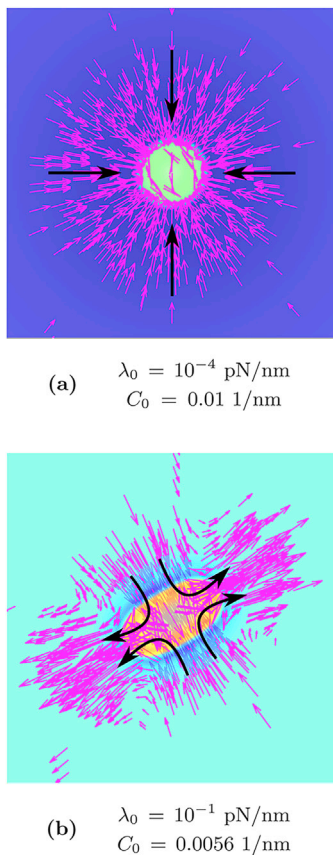


FIGURE 7 Snapshots of membrane shapes and velocity profiles at different resting tensions  $\lambda_0$  from nonaxisymmetric simulations. The overlaid black arrows serve to indicate the character of the flow pattern. In the low resting tension case of  $\lambda_0 = 10^{-4}$  pN/nm, the velocity profile shows inward-pointing radial flow to form a bud. In contrast, in the high resting tension case of  $\lambda_0 = 10^{-1}$  pN/nm, we observe a flow pattern similar to purely extensional flow, with inward-pointing flow along the longer principal axis of the initial ellipse and outward pointing flow along the shorter principal axis of the initial ellipse. To see this figure in color, go online.

does not qualitatively affect the observed membrane shapes. At high resting tensions, the nonaxisymmetric simulations go from shallow pits to cylindrical ridges, whereas the axisymmetric simulations always stall at flat, shallow pits. We note that the spontaneous curvature at which the transition occurs is almost independent of the coat radius. At low resting tensions, both axisymmetric and nonaxisymmetric simulations transition from shallow pits to deep invaginations, and then to buds.

At low resting tension, we can predict the onset of bud formation by considering the geometric deformation of the coated region. We reported above that for a bud,  $H \approx C_0$  in the coated region, which implies the initial coated region deforms into a spherical bud. Equating the initial and final surface areas, we find  $\pi R_0^2 = 4\pi R_{\text{bud}}^2 = 4\pi/(C_0^{\text{bud}})^2$ , from which we approximate

$$C_0^{\text{bud}} \sim \frac{2}{R_0}, \quad (8)$$

Number	Name	Description	Pictograph
I	pit	shallow, axisymmetric deformation	
II	deep invagination	deep, axisymmetric deformation with $z(x=0, y=0) > R_0$	
III	closed bud	deep invaginations with constricted necks	
IV	ridge	non-axisymmetric, flat cylinders	

FIGURE 8 Classification of the morphologies observed in simulations. The pictographs will be used in the morphological “phase” diagrams to indicate the respective morphology. The same pictographs are used in both the axisymmetric and nonaxisymmetric cases for clarity. To see this figure in color, go online.

where  $C_0^{\text{bud}}$  is the spontaneous curvature at which a bud is observed. Equation 8 is plotted as the dashed line in Fig. 9, *a1* and *a2* and reasonably predicts the scaling of the spontaneous curvature required for bud formation. Accordingly, bud formation at low resting tension is a geometrical phenomenon.

#### Resting tension effects: $\lambda_0$ vs. $C_0$

Thus far, we presented simulation results for two extreme cases of the resting tension:  $\lambda_0 = 10^{-4}$  pN/nm and  $\lambda_0 = 10^{-1}$  pN/nm. However, resting tensions in lipid membranes range from  $10^{-1}$  pN/nm in yeast cells (41) to  $3 \times 10^{-3}$  pN/nm in blebbing cells (71,72) and to even lower values in giant unilamellar vesicles (73). Accordingly, we study axisymmetric and nonaxisymmetric membrane morphologies over a wide range of resting tensions. Our results are captured in the morphological “phase” diagrams in Fig. 10, *a1* and *a2*, which show membrane morphologies as the spontaneous curvature is increased, for each value of the resting tension. In Fig. 10, *a1* and *a2*, the spontaneous curvature is increased slowly, such that our simulations correspond to quasistatic equilibrium configurations (Fig. 10, *b* and *c* reveal rate effects associated with changing  $\dot{C}_0$  and are discussed in the subsequent section). This implies that the observed morphologies also minimize the energy of the system.

The nonaxisymmetric simulations shown in Fig. 10 *a1* again show there exist two paths for morphological transitions. At resting tensions below a threshold value of  $\lambda_0 \approx 3 \times 10^{-4}$  pN/nm, membranes transition from shallow pits to deep invaginations and then to spherical buds, with the final morphology compatible with the spherical energy minimization criterion of (5). Above this threshold, on the other hand, membranes transition from shallow pits to ridges, with the latter satisfying the cylindrical energy

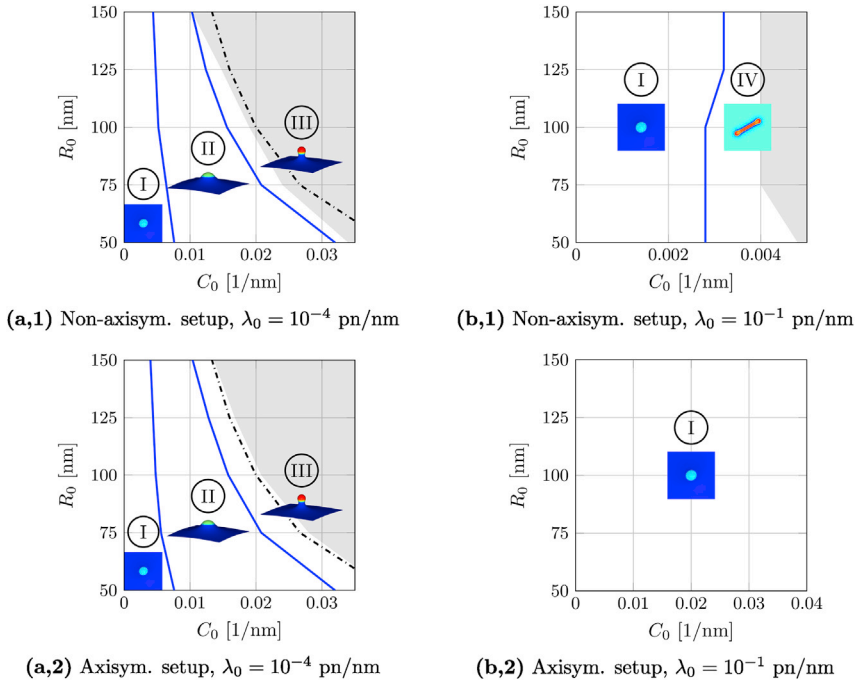


FIGURE 9 Morphological “phase” diagrams: radius of coated region  $R_0$  vs. spontaneous curvature  $C_0$  at different values of the resting tension  $\lambda_0$ , all at the lowest considered rate of spontaneous curvature  $\dot{C}_0^0$ . The shaded areas of the diagrams are not accessible with our numerical framework. In the low resting tension case, there is an inversely proportional relationship between the coated region and spontaneous curvature required for closed buds. The dashed line shows the relationship in Eq. 8, where the proportionality is replaced by an equality. The morphological “phase” diagrams from the axisymmetric and nonaxisymmetric setups agree well. In contrast to the low resting tension case, there is only a mild dependence on the size of the coated region when the resting tension is high and ridges form. The axisymmetric simulations at the high resting tension yield shallow pits at all spontaneous curvatures. To see this figure in color, go online.

minimization criterion of (6). In stark contrast, the axisymmetric simulations shown in Fig. 10 a2 do not have access to the second path to form cylindrical structures; consequently, the simulations stall at shallow pits at resting tensions above  $3 \times 10^{-4}$  pN/nm.

We note that at low resting tensions, below  $\lambda_0 \approx 3 \times 10^{-4}$  pN/nm, the axisymmetric and nonaxisymmetric morphological “phase” diagrams are almost indistinguishable, including the transitions from pits to invaginations to buds. In particular, for a given resting tension, the spontaneous curvatures at which a shallow pit becomes a deep invagination is nearly identical between the two types of simulations. The same is true for the onset of bud formation as well.

#### Rate effects: varying $\dot{C}_0$

In biological and artificial lipid membrane systems, the rate of curvature induction varies in different settings. For example, curvature-inducing proteins can assemble at different rates, thus inducing curvature at different rates as well (13,15). In this section, we study rate effects by changing  $\dot{C}_0$ , the rate of change of spontaneous curvature, on lipid membrane morphologies as a function of the resting tension  $\lambda_0$ . We find that at high resting tensions, higher rates lead to additional viscous stresses in the membrane, and as a result, the observed membrane morphology may not be the lowest-energy configuration.

The results of altering the rate of change of spontaneous curvature  $\dot{C}_0$  are presented in Fig. 10. At low resting tensions, in both the axisymmetric and nonaxisymmetric

cases, membrane morphologies are unaffected by changes in  $\dot{C}_0$ : the transitions from shallow pits to deep invaginations and then to buds are independent of  $\dot{C}_0$ . At high resting tensions, the axisymmetric results are largely independent of  $\dot{C}_0$  as well. However, for nonaxisymmetric simulations at moderate to high resting tensions,  $\dot{C}_0$  strongly affects membrane morphologies, as shown in Fig. 10, a1, b1, and c1. In particular, with increasing rates, the resting tension and spontaneous curvature at which ridges form shift toward higher magnitudes. Hence, the nonaxisymmetric results increasingly resemble the axisymmetric ones when the rate of spontaneous curvature is increased (see Fig. 10, c1 and c2).

To understand why the rate of spontaneous curvature affects our nonaxisymmetric results, we first qualitatively describe the difference in the lipid flow leading to axisymmetric shapes and nonaxisymmetric ridges. At high resting tensions and low rates of change of spontaneous curvature  $\dot{C}_0$ , ridges are low-energy structures, and to form, they require an in-plane shear flow of lipids as seen in Fig. 7 b. Axisymmetric shapes, on the other hand, only draw in lipids radially (Fig. 7 a), thus forming shallow, flat shapes that are energetically unfavorable because of their large bending costs, as discussed previously. We quantify the relative importance of lipid rearrangements and the forced membrane deformations by defining two timescales:

$$\tau_f := \frac{\zeta}{\lambda_0} \quad \text{and} \quad \tau_c := \frac{1}{R_0 \dot{C}_0}, \quad (9)$$

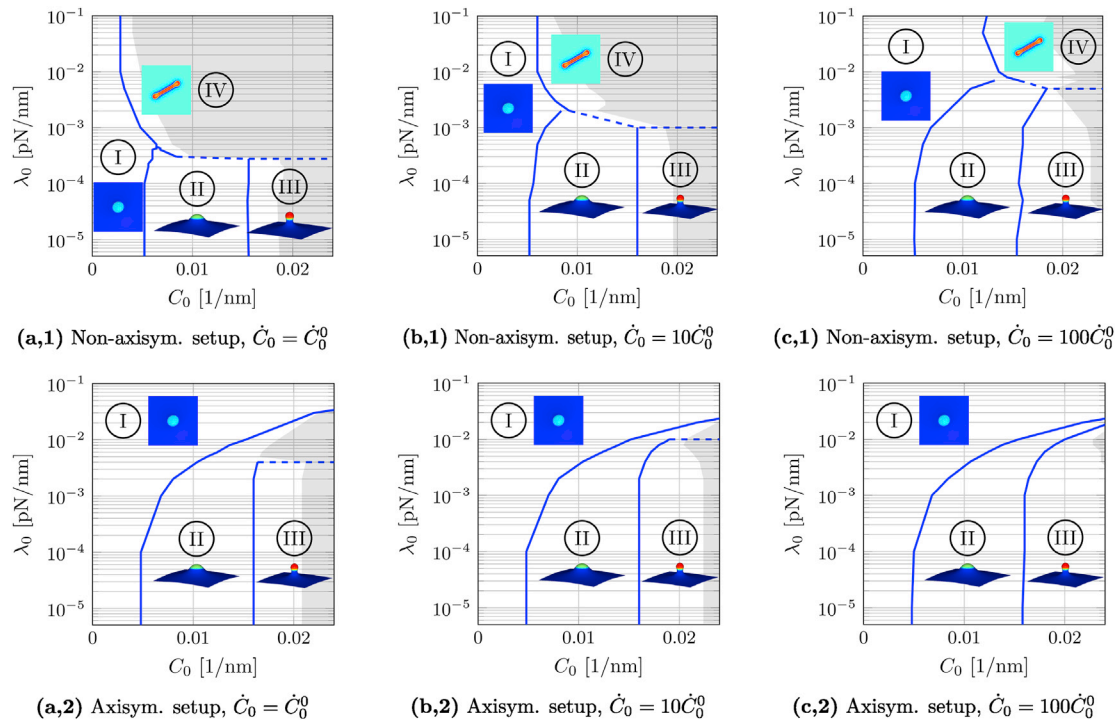


FIGURE 10 Morphological “phase” diagrams: resting tension  $\lambda_0$  vs. spontaneous curvature  $C_0$  at different values of the rate of spontaneous curvature  $\dot{C}_0$ . With increased rate of spontaneous curvature, the resting tension at which ridges are observed increases. The shaded areas of the diagrams are not accessible with our numerical framework. To see this figure in color, go online.

where  $\tau_f$  denotes the timescale associated with out-of-plane deformations and in-plane shear flows (63,65),  $\zeta$  is the two-dimensional intramembrane viscosity, and  $\tau_c$  is a loading timescale associated with the rate of change of spontaneous curvature. When  $\tau_f \ll \tau_c$ , the lipids can quickly rearrange in-plane such that the membrane can find the lowest-energy configurations—which, at high tension, are ridges. As can be easily verified, this condition is satisfied at the lowest rates considered in this study. When  $\tau_f \gg \tau_c$ , on the other hand, lipids are unable to rearrange and access the in-plane shearing modes, and the resulting flow occurs radially in response to the changing isotropic spontaneous curvature. Because the lipids cannot access the in-plane shearing modes, ridges cannot form, and the membrane forms axisymmetric shapes—which are the only available option.

The above arguments on the formation of ridges and axisymmetric shapes also explain the threshold resting tension,  $\lambda_0^{\text{thresh}}$ , which separates ridge formation from the formation of axisymmetric shapes. This threshold is the resting tension at which “phases” I, II, and IV meet (see Fig. 10, *aI*, *bI*, and *cI*). We assume the threshold value occurs when  $\tau_f$  and  $\tau_c$  are comparable, such that (see (9))  $\lambda_0^{\text{thresh}} \sim \zeta R_0 \dot{C}_0$ . Accordingly, increasing  $\dot{C}_0$  by a constant factor should increase  $\lambda_0^{\text{thresh}}$  by the same factor because  $\zeta$  and  $R_0$  are constant. Figure 10, *aI*, *bI*, and *cI* show that when  $\dot{C}_0$  increases by a factor of 10,  $\lambda_0^{\text{thresh}}$  increases roughly by a factor of five. Our simple timescale argument thus predicts the cor-

rect trends for the threshold resting tension in this highly nonlinear dynamical problem. However, a detailed understanding of the effects of  $\dot{C}_0$  and the changes in the morphological “phase” diagrams requires a rigorous stability analysis. We leave such an analysis to a future study.

## DISCUSSION

In this work, we studied lipid membrane morphologies resulting from locally induced curvature. We found axisymmetric solutions at low resting tensions, whereas nonaxisymmetric ridges were observed at high resting tensions. Several previous studies considered the effects of locally induced spontaneous curvature as a means of studying endocytosis (41,43). These works are restricted to axisymmetric shapes and describe a snap-through instability at high tension. Our work, however, contradicts such findings, which neglect lower-energy nonaxisymmetric membrane morphologies.

The nonaxisymmetric lipid membrane shapes observed in this study have implications in understanding biological processes and related phenomena. In relation to endocytosis, for example, experimental studies observe both buds at low resting tensions (14,69) and shallow pits at high resting tensions (74,75). Although the cylindrical ridges we observe at large resting tensions and spontaneous curvatures have not been explicitly reported in stalled endocytic events, there appear to be signatures of such structures in experimental

studies. For example, clathrin is capable of forming cylindrical ridge-like cages in focal adhesions (76), and ridge-like polymerized structures appear to exist in clathrin-mediated endocytosis under hypotonic conditions (75). These observations, in conjunction with our simulation results, suggest a mechanism that allows coat proteins such as clathrin to self-assemble into ridge-like structures at high resting tensions.

Ridge-like structures have also been experimentally observed as eisosomes in yeast cells (77), which are generally under high membrane tension. Although eisosomes are linked to BAR proteins (77), which induce anisotropic curvature (7), our results demonstrate that even isotropic spontaneous curvatures lead to anisotropic cylindrical structures.

Additionally, a recent study found that cholera toxin subunit B binds to the lipid bilayer and induces bud formation (78). The same study suggests that bud formation is inhibited at increased resting tension and reports ridges induced by cholera toxin subunit B (78). However, the correlation between such ridges and the magnitude of the resting tension is not yet known.

Finally, we consider morphological changes accompanying phase separations of biological membranes, in which diffusion of lipids is often negligible. During such processes, budding transitions were found as a result of the different spontaneous curvatures of the phase-separating components (10,79), similar to the structures we found at low resting tension. Furthermore, there is a striking similarity between the ridge-shaped phase separated domains in lipid bilayers (10,12) and the high resting tension ridge structures presented in our study. We speculate that such structures, as observed in (12,80,81), arise because of the membrane being in a high resting tension state, as was also proposed by Harden et al. (82). We hope that our work inspires the careful investigation of the role of resting tension in phase-separating membrane systems with spontaneous curvatures (83).

## SUPPORTING MATERIAL

Supporting Material can be found online at <https://doi.org/10.1016/j.bpj.2020.07.021>.

## AUTHOR CONTRIBUTIONS

Y.A.D.O., A.S., R.A.S., and K.K.M. designed research, performed research, and wrote the manuscript.

## ACKNOWLEDGMENTS

We are grateful to Dr. Joël Tchoufag for many stimulating discussions, and A.S. thanks Mr. Vikash Sahu for assistance with the numerical implementation

K.K.M. and Y.A.D.O. acknowledge the support of the University of California, Berkeley, and National Institutes of Health Grant No. R01-GM110066.

R.A.S. acknowledges the support of the German Research Foundation through Grant No. GSC 111 and the Aachen-California Network for Academic Exchange. A.S. is supported by the Computational Science Graduate Fellowship from the U.S. Department of Energy. Y.A.D.O. was initially supported by the RWTH Scholarship for Doctoral Students and the Aachen-California Network for Academic Exchange.

## REFERENCES

- Doherty, G. J., and H. T. McMahon. 2009. Mechanisms of endocytosis. *Annu. Rev. Biochem.* 78:857–902.
- Baumann, O., and B. Walz. 2001. Endoplasmic reticulum of animal cells and its organization into structural and functional domains. *Int. Rev. Cytol.* 205:149–214.
- Voeltz, G. K., M. M. Rolls, and T. A. Rapoport. 2002. Structural organization of the endoplasmic reticulum. *EMBO Rep.* 3:944–950.
- Sinha, B., D. Köster, ..., P. Nassoy. 2011. Cells respond to mechanical stress by rapid disassembly of caveolae. *Cell.* 144:402–413.
- Heuser, J. 1980. Three-dimensional visualization of coated vesicle formation in fibroblasts. *J. Cell Biol.* 84:560–583.
- Ford, M. G., I. G. Mills, ..., H. T. McMahon. 2002. Curvature of clathrin-coated pits driven by epsin. *Nature.* 419:361–366.
- McMahon, H. T., and J. L. Gallop. 2005. Membrane curvature and mechanisms of dynamic cell membrane remodeling. *Nature.* 438:590–596.
- Zimmerberg, J., and M. M. Kozlov. 2006. How proteins produce cellular membrane curvature. *Nat. Rev. Mol. Cell Biol.* 7:9–19.
- Ali Doosti, B., W. Pezeshkian, ..., T. Lobovkina. 2017. Membrane tubulation in lipid vesicles triggered by the local application of calcium ions. *Langmuir.* 33:11010–11017.
- Baumgart, T., S. T. Hess, and W. W. Webb. 2003. Imaging coexisting fluid domains in biomembrane models coupling curvature and line tension. *Nature.* 425:821–824.
- Zidovska, A., K. K. Ewert, ..., C. R. Safinya. 2009. Block liposomes from curvature-stabilizing lipids: connected nanotubes, -rods, or -spheres. *Langmuir.* 25:2979–2985.
- Rozovsky, S., Y. Kaizuka, and J. T. Groves. 2005. Formation and spatio-temporal evolution of periodic structures in lipid bilayers. *J. Am. Chem. Soc.* 127:36–37.
- Liu, J., Y. Sun, ..., G. F. Oster. 2009. The mechanochemistry of endocytosis. *PLoS Biol.* 7:e1000204.
- Kukulski, W., M. Schorb, ..., J. A. Briggs. 2012. Plasma membrane reshaping during endocytosis is revealed by time-resolved electron tomography. *Cell.* 150:508–520.
- Watanabe, S., B. R. Rost, ..., E. M. Jorgensen. 2013. Ultrafast endocytosis at mouse hippocampal synapses. *Nature.* 504:242–247.
- Canham, P. B. 1970. The minimum energy of bending as a possible explanation of the biconcave shape of the human red blood cell. *J. Theor. Biol.* 26:61–81.
- Helfrich, W. 1973. Elastic properties of lipid bilayers: theory and possible experiments. *Z. Naturforsch. C.* 28:693–703.
- Evans, E. A. 1974. Bending resistance and chemically induced moments in membrane bilayers. *Biophys. J.* 14:923–931.
- Naghdi, P. M. 1973. *The Theory of Shells and Plates*. Springer, Berlin, Germany.
- Deuling, H., and W. Helfrich. 1976. The curvature elasticity of fluid membranes: a catalogue of vesicle shapes. *J. Phys. (Paris).* 37:1335–1345.
- Seifert, U., K. Berndl, and R. Lipowsky. 1991. Shape transformations of vesicles: phase diagram for spontaneous-curvature and bilayer-coupling models. *Phys. Rev. A.* 44:1182–1202.
- Wintz, W., H.-G. Döbereiner, and U. Seifert. 1996. Starfish vesicles. *Europhys. Lett.* 33:403.

23. Barrett, J. W., H. Garcke, and R. Nürnberg. 2015. Numerical computations of the dynamics of fluidic membranes and vesicles. *Phys. Rev. E Stat. Nonlin. Soft Matter Phys.* 92:052704.
24. Derényi, I., F. Jülicher, and J. Prost. 2002. Formation and interaction of membrane tubes. *Phys. Rev. Lett.* 88:238101.
25. Cuvelier, D., I. Derényi, ..., P. Nassoy. 2005. Coalescence of membrane tethers: experiments, theory, and applications. *Biophys. J.* 88:2714–2726.
26. Seifert, U. 1993. Curvature-induced lateral phase segregation in two-component vesicles. *Phys. Rev. Lett.* 70:1335–1338.
27. Allain, J.-M., and M. Ben Amar. 2006. Budding and fission of a multi-phase vesicle. *Eur Phys J E Soft Matter.* 20:409–420.
28. Nowak, S. A., and T. Chou. 2008. Membrane lipid segregation in endocytosis. *Phys. Rev. E Stat. Nonlin. Soft Matter Phys.* 78:021908.
29. Idema, T., and C. Storm. 2011. Analytical expressions for the shape of axisymmetric membranes with multiple domains. *Eur Phys J E Soft Matter.* 34:67.
30. Mercker, M., A. Marciniak-Czochra, ..., D. Hartmann. 2013. Modeling and computing of deformation dynamics of inhomogeneous biological surfaces. *SIAM J. Appl. Math.* 73:1768–1792.
31. Kim, K. S., J. Neu, and G. Oster. 1998. Curvature-mediated interactions between membrane proteins. *Biophys. J.* 75:2274–2291.
32. Agrawal, A., and D. J. Steigmann. 2009. Modeling protein-mediated morphology in biomembranes. *Biomech. Model. Mechanobiol.* 8:371–379.
33. Rangamani, P., K. K. Mandadapu, and G. Oster. 2014. Protein-induced membrane curvature alters local membrane tension. *Biophys. J.* 107:751–762.
34. Sigurdsson, J. K., and P. J. Aatzberger. 2016. Hydrodynamic coupling of particle inclusions embedded in curved lipid bilayer membranes. *Soft Matter.* 12:6685–6707.
35. Morris, R. G. 2017. Signatures of mechanosensitive gating. *Biophys. J.* 112:3–9.
36. Deslandes, F., A. R. Thiam, and L. Forêt. 2017. Lipid droplets can spontaneously bud off from a symmetric bilayer. *Biophys. J.* 113:15–18.
37. Choudhary, V., G. Golani, ..., M. M. Kozlov. 2018. Architecture of lipid droplets in endoplasmic reticulum is determined by phospholipid intrinsic curvature. *Curr. Biol.* 28:915–926.e9.
38. Agrawal, N. J., J. Nukpezah, and R. Radhakrishnan. 2010. Minimal mesoscale model for protein-mediated vesiculation in clathrin-dependent endocytosis. *PLoS Comput. Biol.* 6:e1000926.
39. Liu, J., M. Kaksonen, ..., G. Oster. 2006. Endocytic vesicle scission by lipid phase boundary forces. *Proc. Natl. Acad. Sci. USA.* 103:10277–10282.
40. Dmitrieff, S., and F. Nédélec. 2015. Membrane mechanics of endocytosis in cells with turgor. *PLoS Comput. Biol.* 11:e1004538.
41. Walani, N., J. Torres, and A. Agrawal. 2015. Endocytic proteins drive vesicle growth via instability in high membrane tension environment. *Proc. Natl. Acad. Sci. USA.* 112:E1423–E1432.
42. Lowengrub, J., J. Allard, and S. Aland. 2016. Numerical simulation of endocytosis: viscous flow driven by membranes with non-uniformly distributed curvature-inducing molecules. *J. Comput. Phys.* 309:112–128.
43. Hassinger, J. E., G. Oster, ..., P. Rangamani. 2017. Design principles for robust vesiculation in clathrin-mediated endocytosis. *Proc. Natl. Acad. Sci. USA.* 114:E1118–E1127.
44. Ma, R., and J. Berro. 2019. Mechanics of membrane internalization against osmotic pressure: boundary conditions make a difference. *bioRxiv* <https://doi.org/10.1101/558890v1>.
45. Laradji, M., and P. B. Sunil Kumar. 2004. Dynamics of domain growth in self-assembled fluid vesicles. *Phys. Rev. Lett.* 93:198105.
46. McWhirter, J. L., G. Ayton, and G. A. Voth. 2004. Coupling field theory with mesoscopic dynamical simulations of multicomponent lipid bilayers. *Biophys. J.* 87:3242–3263.
47. Sunil Kumar, P. B., G. Gompper, and R. Lipowsky. 2001. Budding dynamics of multicomponent membranes. *Phys. Rev. Lett.* 86:3911–3914.
48. Ayton, G. S., J. L. McWhirter, ..., G. A. Voth. 2005. Coupling field theory with continuum mechanics: a simulation of domain formation in giant unilamellar vesicles. *Biophys. J.* 88:3855–3869.
49. Weinstein, J., and R. Radhakrishnan. 2006. ‘KMC-TDGL’-a coarse-grained methodology for simulating interfacial dynamics in complex fluids: application to protein-mediated membrane processes. *Mol. Phys.* 104:3653–3666.
50. Reynwar, B. J., G. Illya, ..., M. Deserno. 2007. Aggregation and vesiculation of membrane proteins by curvature-mediated interactions. *Nature.* 447:461–464.
51. Liu, J., R. Tourdot, ..., R. Radhakrishnan. 2012. Mesoscale simulations of curvature-inducing protein partitioning on lipid bilayer membranes in the presence of mean curvature fields. *Mol. Phys.* 110:1127–1137.
52. Tourdot, R., J. Liu, and R. Radhakrishnan. 2012. Mesoscale simulations of curvature inducing protein partitioning in the presence of mean curvature gradients. In 2012 38th Annual Northeast Bioengineering Conference (NEBEC). IEEE, pp. 366–367.
53. Tourdot, R. W., R. P. Bradley, ..., R. Radhakrishnan. 2014. Multiscale computational models in physical systems biology of intracellular trafficking. *IET Syst. Biol.* 8:198–213.
54. Sreeja, K. K., J. H. Ipsen, and P. B. Sunil Kumar. 2015. Monte Carlo simulations of fluid vesicles. *J. Phys. Condens. Matter.* 27:273104.
55. Ramakrishnan, N., R. P. Bradley, ..., R. Radhakrishnan. 2018. Biophysics of membrane curvature remodeling at molecular and mesoscopic length scales. *J. Phys. Condens. Matter.* 30:273001.
56. Arroyo, M., and A. Desimone. 2009. Relaxation dynamics of fluid membranes. *Phys. Rev. E Stat. Nonlin. Soft Matter Phys.* 79:031915.
57. Rangamani, P., A. Agrawal, ..., D. J. Steigmann. 2013. Interaction between surface shape and intra-surface viscous flow on lipid membranes. *Biomech. Model. Mechanobiol.* 12:833–845.
58. Sauer, R. A., and T. X. Duong. 2017. On the theoretical foundations of thin solid and liquid shells. *Math. Mech. Solids.* 22:343–371.
59. Sahu, A., R. A. Sauer, and K. K. Mandadapu. 2017. Irreversible thermodynamics of curved lipid membranes. *Phys. Rev. E.* 96:042409.
60. Ma, L., and W. S. Klug. 2008. Viscous regularization and r-adaptive remeshing for finite element analysis of lipid membrane mechanics. *J. Comput. Phys.* 227:5816–5835.
61. Sauer, R. A., T. X. Duong, ..., D. J. Steigmann. 2017. A stabilized finite element formulation for liquid shells and its application to lipid bilayers. *J. Comput. Phys.* 330:436–466.
62. Duong, T. X., F. Roohbakhshan, and R. A. Sauer. 2017. A new rotation-free isogeometric thin shell formulation and a corresponding continuity constraint for patch boundaries. *Comput. Methods Appl. Mech. Eng.* 316:43–83.
63. Sahu, A., Y. A. Omar, ..., K. K. Mandadapu. 2020. Arbitrary Lagrangian–Eulerian finite element method for curved and deforming surfaces: I. General theory and application to fluid interfaces. *J. Comp. Phys.* 407:109253.
64. Torres-Sánchez, A., D. Millán, and M. Arroyo. 2019. Modelling fluid deformable surfaces with an emphasis on biological interfaces. *J. Fluid Mech.* 872:218–271.
65. Sahu, A., A. Glisman, ..., K. K. Mandadapu. 2020. Geometry and dynamics of lipid membranes: the Scriven-Love number. *Phys. Rev. E.* 101:052401.
66. Evans, E. A., and R. Skalak. 1980. *Mechanics and Thermodynamics of Biomembranes.* CRC Press, Boca Raton, FL.
67. Seifert, U., and S. A. Langer. 1993. Viscous modes of fluid bilayer membranes. *Europhys. Lett.* 23:71.
68. Rahimi, M., and M. Arroyo. 2012. Shape dynamics, lipid hydrodynamics, and the complex viscoelasticity of bilayer membranes [corrected]. *Phys. Rev. E Stat. Nonlin. Soft Matter Phys.* 86:011932.

69. Heuser, J. E., and R. G. Anderson. 1989. Hypertonic media inhibit receptor-mediated endocytosis by blocking clathrin-coated pit formation. *J. Cell Biol.* 108:389–400.
70. Wiese, W., W. Harbich, and W. Helfrich. 1992. Budding of lipid bilayer vesicles and flat membranes. *J. Phys. Condens. Matter.* 4:1647.
71. Dai, J., M. P. Sheetz, ..., C. E. Morris. 1998. Membrane tension in swelling and shrinking molluscan neurons. *J. Neurosci.* 18:6681–6692.
72. Dai, J., and M. P. Sheetz. 1999. Membrane tether formation from blebbing cells. *Biophys. J.* 77:3363–3370.
73. Pécéréaux, J., H.-G. Döbereiner, ..., P. Bassereau. 2004. Refined contour analysis of giant unilamellar vesicles. *Eur Phys J E Soft Matter.* 13:277–290.
74. Boulant, S., C. Kural, ..., T. Kirchhausen. 2011. Actin dynamics counteract membrane tension during clathrin-mediated endocytosis. *Nat. Cell Biol.* 13:1124–1131.
75. Saleem, M., S. Morlot, ..., A. Roux. 2015. A balance between membrane elasticity and polymerization energy sets the shape of spherical clathrin coats. *Nat. Commun.* 6:6249.
76. Elkhatib, N., E. Bresteau, ..., G. Montagnac. 2017. Tubular clathrin/AP-2 lattices pinch collagen fibers to support 3D cell migration. *Science.* 356:eaa14713.
77. Lee, J.-H., J. E. Heuser, ..., U. Goodenough. 2015. Eisosome ultrastructure and evolution in fungi, microalgae, and lichens. *Eukaryot. Cell.* 14:1017–1042.
78. Kabbani, A. M., and C. V. Kelly. 2017. Nanoscale membrane budding induced by CTxB and detected via polarized localization microscopy. *Biophys. J.* 113:1795–1806.
79. Veatch, S. L., and S. L. Keller. 2003. Separation of liquid phases in giant vesicles of ternary mixtures of phospholipids and cholesterol. *Biophys. J.* 85:3074–3083.
80. Li, L., and J.-X. Cheng. 2006. Coexisting stripe- and patch-shaped domains in giant unilamellar vesicles. *Biochemistry.* 45:11819–11826.
81. Chen, D., and M. M. Santore. 2014. Large effect of membrane tension on the fluid-solid phase transitions of two-component phosphatidylcholine vesicles. *Proc. Natl. Acad. Sci. USA.* 111:179–184.
82. Harden, J. L., F. C. Mackintosh, and P. D. Olmsted. 2005. Budding and domain shape transformations in mixed lipid films and bilayer membranes. *Phys. Rev. E Stat. Nonlin. Soft Matter Phys.* 72:011903.
83. Cornell, C. E., A. D. Skinkle, ..., S. L. Keller. 2018. Tuning length scales of small domains in cell-derived membranes and synthetic model membranes. *Biophys. J.* 115:690–701.
84. Boal, D., and D. H. Boal. 2012. *Mechanics of the Cell.* University Press, Cambridge.
85. Siegel, D. P., and M. M. Kozlov. 2004. The Gaussian curvature elastic modulus of N-monomethylated dioleoylphosphatidylethanolamine: relevance to membrane fusion and lipid phase behavior. *Biophys. J.* 87:366–374.
86. Ehrlich, M., W. Boll, ..., T. Kirchhausen. 2004. Endocytosis by random initiation and stabilization of clathrin-coated pits. *Cell.* 118:591–605.
87. Cicuta, P., S. L. Keller, and S. L. Veatch. 2007. Diffusion of liquid domains in lipid bilayer membranes. *J. Phys. Chem. B.* 111:3328–3331.
88. Avinoam, O., M. Schorb, ..., M. Kaksonen. 2015. ENDOCYTOSIS. Endocytic sites mature by continuous bending and remodeling of the clathrin coat. *Science.* 348:1369–1372.